A vision-based soft somatosensory system for distributed pressure and temperature sensing

Chen Yu, Lukas Lindenroth, Jian Hu, Junghwan Back, George Abrahams, Hongbin Liu*

Abstract— **Emulating a human-like somatosensory system in instruments such as robotic hands and surgical grippers has the potential to revolutionize these domains. Using a combination of different sensing modalities is problematic due to the limited space and incompatibility of these sensing principles. Therefore, in contrast to the natural world, it is currently difficult to concurrently measure the force, geometry, and temperature of contact in conventional tactile sensing. To this end, here we present a soft multifunctional tactile sensing principle. The temperature is estimated using a thermochromic liquid crystal ink layer which exhibits colour variation under temperature change. The shape and force of contact is estimated through the 3D reconstruction of a deformed soft silicone surface. Our experiments have demonstrated high accuracy in all three modalities, which can be measured at the same time. The resolution of the distributed force and temperature sensing was found to be 0.7N and 0.4℃ respectively.**

Index Terms – Tactile sensing, Temperature sensing, Soft material.

I. INTRODUCTION

The somatosensory system of human provides sensation such as pressure and temperature which can occur anywhere in the body, in contrast to localized sensation such as sight, hearing. Human heavily rely on the somatosensory system to physically interact with unstructured environments and recognise objects. To date, numerous research efforts have been carried out to recreate the artificial tactile sensing system and achieved significantly progress. To mimic human skills, softness is one of the requirements for tactile sensing due to various benefits it can introduce. A large number of soft tactile sensors have been developed in recent years. Here, based on different principles of sensing, existing soft tactile sensors are divided into electrical-based type, magnetic field-based type and vision-based type. Electrical-based soft tactile sensors mainly utilize piezoelectric and piezo-resistive effects [1]. The underlying mechanism is that material deformation will introduce resistance change, from which contact force can be inferred [2]. In some research, piezo-resistive material is arranged into soft arrays so that distributed force sensing can be achieved [3]. Due to the softness of piezo-resistive material, the tactile sensing array can be made into various shapes then be embedded in wearable instruments [4]. Capacitive tactile sensors use a soft dielectric to introduce capacitance variation that is proportional to potential changes [5] [6]. However, due to the distribution of conductive cables, the size and sensing area of electrical-based tactile sensing is limited. Magnetic tactile sensors use magnetic field intensity and direction to estimate contact force [7] and contact shape [8]. Magnets are often embedded in soft silicon tips. Once the soft tips move, the magnetic sensing points can estimate contact force and shape by analyzing magnetic field variation [9] [10]. To improve the softness, some of the rigid magnets is replaced by magnetic soft elastomer [11]. However, magnetic-based tactile sensing is susceptible to interference, which limits the range of applications. Furthermore, there is a significant technological challenge in increasing the density or spatial resolution of tactile sensing for the above-mentioned sensing methods.

A promising approach to obtaining high spatial resolution in soft tactile sensing is based on internal visual measurements and the subsequent conversion from deformation of an elastic component to distributed pressure information [12]. To enhance the deformation characteristics, existing methods either apply photometric stereo algorithms to a soft layer such as the Gelsight technology [13][14], or employ dot-cloud structures on soft elastomer as exemplified by the Tactip [15][16]. Distributed contact information is estimated by marker tracking algorithms [17]. These methods successfully enable distributed tactile sensing while retaining the required softness of the sensor. However how to integrate distributed tactile sensing and temperature sensing ability together to mimic the full human level somatosensory system is still an open question and no result has been reported to this challenge. In this paper, we introduce a novel vision-based sensing principle which can simultaneously measure densely distributed tactile and temperature information on a soft

*indicates the corresponding author, email: Hongbin.liu@kcl.ac.uk.

The authors Chen Yu, Jian Hu, Junghwan Back, George Abrahams and Hongbin Liu are with School of Biomedical Engineering and Imaging Sciences, King's college London, UK. The author Lukas Lindenroth is with the Department of Engineering, King's College London, UK.

Acknowledgement: This work is sponsored by China Scholarship Council. (CSC NO.201808060382) and the National Natural Science Foundation of China (NSFC) No.51520105006.

material. We created a soft layer consisting of thermochromic liquid crystals (TLC) link to measure temperature changes. To enhance the temperature sensitivity and in the same time without reducing the spatial resolution of tactile sensing, we implemented the TLC material to form line grating patterns and applied an image-based 3D reconstruction algorithm which is used to estimate pressure distribution, and then interpolate contact force and contact shape. The temperature distribution is measured by the hue value of individual pixel colours from the image. To prove the principle, we develop a soft fingertip and carried out experiments to validate the performance of tactile and temperature sensing. The results of the experiments conducted in this work indicate that fingertip can measure distributed force and temperature with high accuracy. The force sensing resolution is around 0.7N, which is about 4.6% of the sensing range (from 0N to 15N). The temperature sensing resolution is around 0.4 ℃, which is about 6.7% of the sensing range (from 25℃ to 31℃).

II. SENSING PRINCIPLE AND MANUFACTURE

A. Objective

The main objective of this sensing method is to imitate the somatosensory system as found in human skin, which can sense contact force, contact shape and surface temperature simultaneously with the contact surface being self-adaptive over a small area. In order to achieve the artificial human-like haptic sensing, the new sensing principle needs to comprise of an elastic and deformable surface, high sensing density and is the capability to measure distributed pressure and temperature information. In addition, the pressure and temperature sensing need to be independent of each other.

B. Image-based 3D reconstruction for haptic sensing

In this paper, a method based on Fourier Transform Profilometry (FTP) is used to detect and digitalize the Physical deformation. As a mature 3D shape detection method, the mathematical and algorithmic background of this widely adopted approach is shown in [18]. In this method, a projector is used to create light fringe patterns on an object's surface and a camera is used to collect the deformed grating images. In this tactile sensor, instead of projecting light fringes on a surface, a black and white grated silicon layer is created. Once deformed, the grates on the rubber layer, considered as a Fourier series expansion in this method, will exhibit a phase shift. By using FTP, the phase shift of the pattern can be converted into height variation, which can be integrated into contact shape change.

As shown in Fig 1 (a), the cured grating black silicon base is filled with liquid form white silicon rubber and then be cured again. This procedure ensures elasticity of the silicon layer. The width of grate is 0.5mm. In Fig 1(b), one grated silicon layer which has been pressed and captured using the attached camera is presented. By using the FTP algorithm, the phase differences among the deformed grates have been calculated and the 3D phase unwrapping method based on

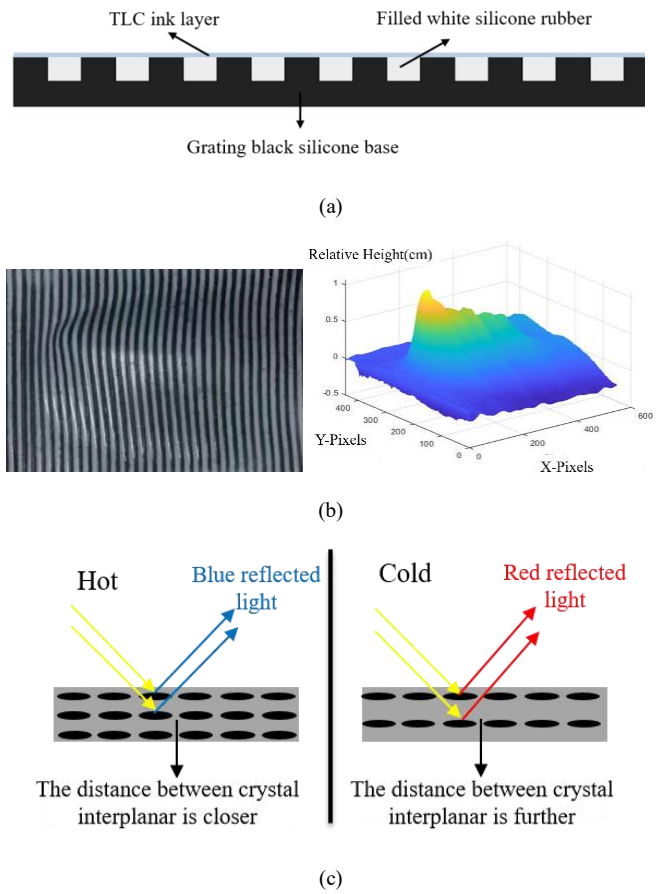

Fig. 1 (a) Cross section of grating layer. (b) Pressed elastic grating silicon rubber layer and the corresponding image-based 3D reconstruction results by FTP method. (c) Principle of TLC ink for temperature sensing.

phase differences has been applied [19]. Then, the deformation of the soft silicone layer, which equals to the relative height of the corresponding location, is 3D reconstructed using the FTP algorithm. According to the FTP algorithm, there is a positive correlation between density of grates and resolution of the shape, thus the performance of 3D reconstruction can be improved by increasing the density of grates on the silicone layer. Moreover, the accuracy of the 3D reconstruction, which determines the resolution of the tactile sensing, can be influenced by the image resolution [20]. Therefore, the resolution of the sensing method can be improved by using the high-resolution image acquisition instruments.

C. Thermochromic liquid crystal (TLC) ink

Liquid crystal is widely used in electronic displays such as pocket calculator, electronic watch and LCD Televisions. Liquid crystals have the properties of liquid in some respects and properties of solid in others. The functional liquid crystal has the special forms named nematic, smectic and cholestic [21]. For common liquid crystal, under certain environment conditions, liquid crystal molecules are lined up and ensure special properties of liquid crystal layer. Once the environment, such as electrical field, temperature, light intensity and light wavelength, has changed, the liquid crystal layer will have variation on the macro level due to the

molecular orientation transformation and distance change on molecular level.

TLC ink is sensitive to temperature which due to the liquid crystals can form into a number of different phases. When temperature is lower or higher than a certain range, the molecules are formed in smectic phase or isotropic state and the layer will be transparent. Once the temperature varies in the working range, the distance between molecules will change, which makes the wavelength of reflected light vary [22].

As shown in Fig.1 (c), within the operating temperature range, the molecular property of the TLC is related to the temperature, which is shown as colour on the macro level. When the temperature of the TLC layer is out of the operating temperature range, the layer is transparent and does not exhibit any colour. Within the operating temperature range, once the temperature of the TLC layer increases, the wavelength of the reflected light decreases and the colour of TLC layer appears. The colour of the TLC layer changes from red to purple to thespectrum of visible light when its temperature increases from the lower limit to the higher limit of the temperature range.

Although the TLC layer exhibits colour variation when the temperature is within operating temperature range, the deformation of the grates is still visible in the image. When the sensing layer is used to detect distributed pressure, the original deformed grating images are converted to grayscale images to minimize the influence of colour variation. Although the colour variation can change the grayscale value of pixels in the images, after applying the FTP algorithm, the corresponding error caused by colour variation in the 3D reconstruction outcome is negligible. At the same time, the same original images will be used to detect the temperature distribution by analyzing the distribution of colour. Therefore, the method of pressure sensing and the method of surface temperature sensing can work independently. As a liquid crystal material, the fully functional TLC layer can be extremely thin, which ensures fast heat conduction. Also, the flexibility of TLC layer ensures that the temperature sensing unit will not be damaged by deformation. In this case, the TLC ink can be used as the temperature sensing unit.

D. Integration of sensing principle

To integrate the tactile and temperature sensing principle, a novel multifunction sensor has been developed. This sensor can be divided into two parts: the sensing part and the data acquisition part. The sensing part is made of soft silicone rubber as shown in Fig 2. It consists of three soft parts: a sensing layer, transparent silicone filler and TLC coating between the two. The sensing layer is a curved surface silicone layer, which is made of highly elastic silicone rubber (Dragon Skin 20, Smooth-on) mixed with black and white silicone dye. The sensing layer is fingertip-shaped so that it has larger contact and sensing area. The transparent elastic silicone rubber (Solaris, Smooth-on) filler is directly cured inside the sensing layer so that the air-gap and trapped air can be eliminated. The transparency of the silicone rubber filler ensures the accuracy of image transmission. Between the sensing layer and filler, there is a transparent coating layer made of TLC material, which allows for temperature sensing in the tactile sensor. Before injecting the liquid transparent silicon, TLC ink is evenly applied to the inside surface of the sensing layer and cured at room temperature. Then after injecting and curing the liquid transparent silicone filler, the TLC coating layer can be tightly bonded between two elastomers so that it cannot be damaged when the soft part is compressed. The thickness of the sensing layer influences speed of heat conduction, and therefore the fingertip-shaped sensing layer is fabricated at a thickness of 1mm to ensure the speed of heat conduction.

Inside the structure, a piece of clear acrylic sheet is used to support the soft sensing part. Underneath the clear acrylic sheet, a piece of mirror is attached to the sensor body, by which the tactile and temperature information can be transferred to the camera in the aperture of the structure for data processing.

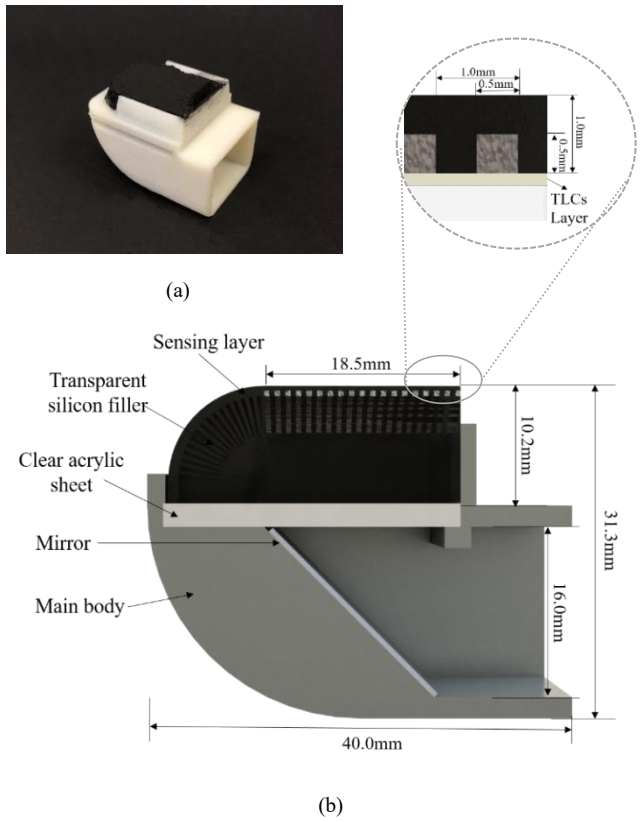

Fig. 2 (a) Tactile/temperature senor. (b) Cross-section view and zoom-in view of sensor

E. Data processing algorithm

The FTP algorithm for 3D reconstructing the deformation is written in MATLAB. In the FTP algorithm, the deformed grating images are firstly converted to grayscale image, I_g (dim n×m). 2D fast Fourier transform algorithm (2D FFT) was applied to I_g, convert it to a matrix A_1 (dim n×m), which contains frequency domain information. The matrix A_1 is rearranged by shifting the zero-frequency component to the center. The "fftshift" command is used in this procedure. Then, in matrix A_1, desired frequency components are maintained while the other frequency

components are set to 0. Therefore, the new matrix A_2 (dim n×m) are created to extract the deformation of grating image from matrix A_1. Then, the 2D inverse fast Fourier transform algorithm (2D IFFT) is applied to A_2 to create A_3 (dim n×m). According to the FTP algorithm, the elements in A_3 are complex numbers. The absolute phase value of each complex number represents the height of the deformation and is subsequently used to create the matrix A_4 (dim n×m). After filtering high frequency noise, the matrix A_4 is used to represent the 3D reconstruction of the deformation.

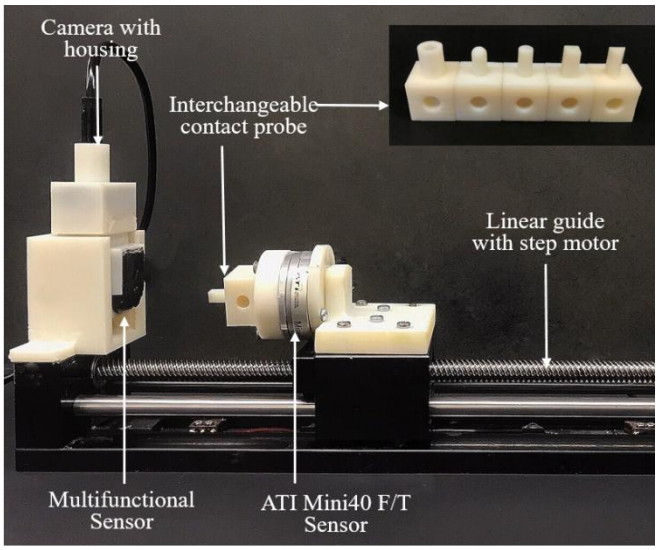

Fig. 3 Contact shape and force experimental setup

TABLE. 1 THE DESIGN OF DIFFERENT INDENTERS

The shape of indenter	The contact area of indenter [cm ^{2}]	Picture of indenter
Round	0.1932	
Square	0.25	
Annulus	0.3063	
Triangle	0.1951	

III. EXPERIMENTS AND RESULTS

An overview of the experimental setup is shown in Fig 3. The sensor is fixed to a connector which is attached to the end of linear guide. A camera with cylindrical housing is fixed to the end of the sensor to capture the desired image. A 6-axis force/torque sensor (ATI Mini 40) is fixed on the mobile part of linear guide, on the surface of which interchangeable contact indenters with different shapes and sizes can be attached. There are five types of indenters which have an annulus, a spherical, a round, a square and a triangular surface, as shown in table 1. The indentation distance is controlled by the linear guide with a stepper motor and the real time reference force values are recorded.

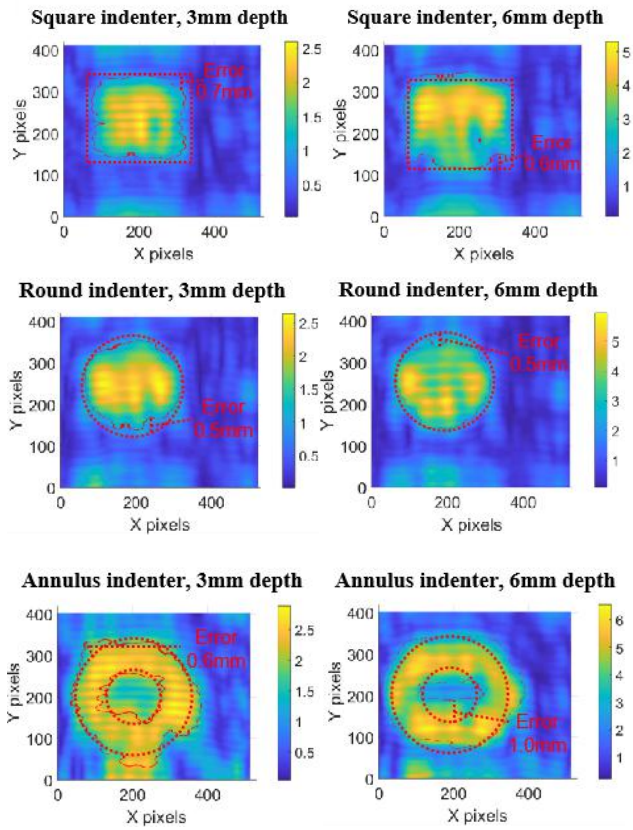

Fig. 4 3D reconstructed indentation with different shapes (The red solid lines indicate the estimated contact shapes and the red dotted lines indicate the actual contact area of the indenters).

A. Contact shape sensing

To investigate the contact shape sensing ability of the sensor, the round, square and annulus indenters listed in table 1 were used to indent the soft layer from 3mm to 6mm depth. Each test was carried out once. The figures shown in Fig. 4 show the depth map of the 3D reconstructed layer deformations. Based on experimental observations, a threshold value of 80 percent of the maximum height of the deformation is used to determine the contour of the indenter shape. As shown in Fig. 4, the red solid lines indicate the estimated contact shapes and the red dotted lines indicate the actual contact shapes. In each figure, the maximum error between actual and estimated shape has been analyzed and marked in the figures. From the 3D reconstructed indentations, we observe that the contact area accuracy is about 1mm based on the current sensor design.

The spatial resolution of this sensing principle is linked to the imaging resolution. It also depends on the elastic material properties of the layer. A more in-depth theoretical analysis of the area resolution of the force sensing will be carried out in future work.

B. *Contact force sensing*

To investigate the contact force sensing ability of the sensor, the 4 indenters listed in table 1 are used to conduct surface indentation tests. For each indenter, the indentation depth ranges from 0.5mm to 12mm, with a 0.5mm increment. The force value and the surface deformation were recorded for each indentation increment. For each indenter, the above-described test protocol was repeated twice. By comparing the 3D reconstructed indentation depth, contact area and true force value, a force estimation formulation has been derived.

To quantify the relationship between the indentation depth and the contact force, the 3D reconstructed indentation depth is firstly calculated. The estimated indentation depth of one image is determined by the averaging the top 5% deformation depths obtained from the 3D reconstruction algorithm.A comparison between estimated indentation depth and real indentation depth is shown in Fig. 5(b).

According to generalized Hooke's Law, within the linear elastic range of the material, the unidirectional compression deformation of a solid is proportional to the external force applied. To be specific, the mathematical relationship can be described as:

$$\varepsilon_x = \frac{1}{E}[\sigma_x - v(\sigma_y + \sigma_z)] \quad (1)$$

$$\varepsilon_y = \frac{1}{E}[\sigma_y - v(\sigma_x + \sigma_z)] \quad (2)$$

$$\varepsilon_z = \frac{1}{E}[\sigma_z - v(\sigma_x + \sigma_y)] \quad (3)$$

Where the $\varepsilon_i(\mathrm{i} = \mathrm{x,y,z})$ stands for normal strain from 3 directions and $\sigma_i(i = x,y,z)$ represents corresponding normal stress. E is the Young's modulus of elastomer and v is Poisson's ratio of the elastomer. In these experiments, because the indentation is generated perpendicular to contact surface, the shear stress and shear strain is ignored. As shown in Fig.2(a), due to the constraint around the soft part, the normal strain from x axis and y axis can be ignored. Therefore, the relationship between normal stain and normal stress along z axis can be simplified as:

$$\varepsilon_z = \frac{1}{E}\sigma_z \quad (4)$$

Where,

$$\varepsilon_z = \Delta v / v$$

$$\sigma_z = F_z / s$$

As the contact shape is constant during one experiment, $\Delta v/v$ is equivalent to $\Delta l/l$. Therefore, formula (4) can be further simplified to:

$$F_z = A \cdot E \cdot \frac{\Delta l}{l} \quad (5)$$

In this equation, the young's modular (E) and height (l) of soft part in this tactile sensor is fixed therefore can be considered as a coefficient(k). Then it is clearly shown that the contact force is proportional to the product of contact area (A) and indentation depth (Δl), which is known as indentation volume (ΔV). Therefore, the relationship between estimated contact force and estimated indentation volume can be described as:

$$F_z = k \cdot \Delta V \quad (6)$$

According to the design specifications, the contact area of each contact indenter is shown in Table.1. By multiplying estimated indentation depth and the corresponding contact area, the estimated indentation volume can be acquired.

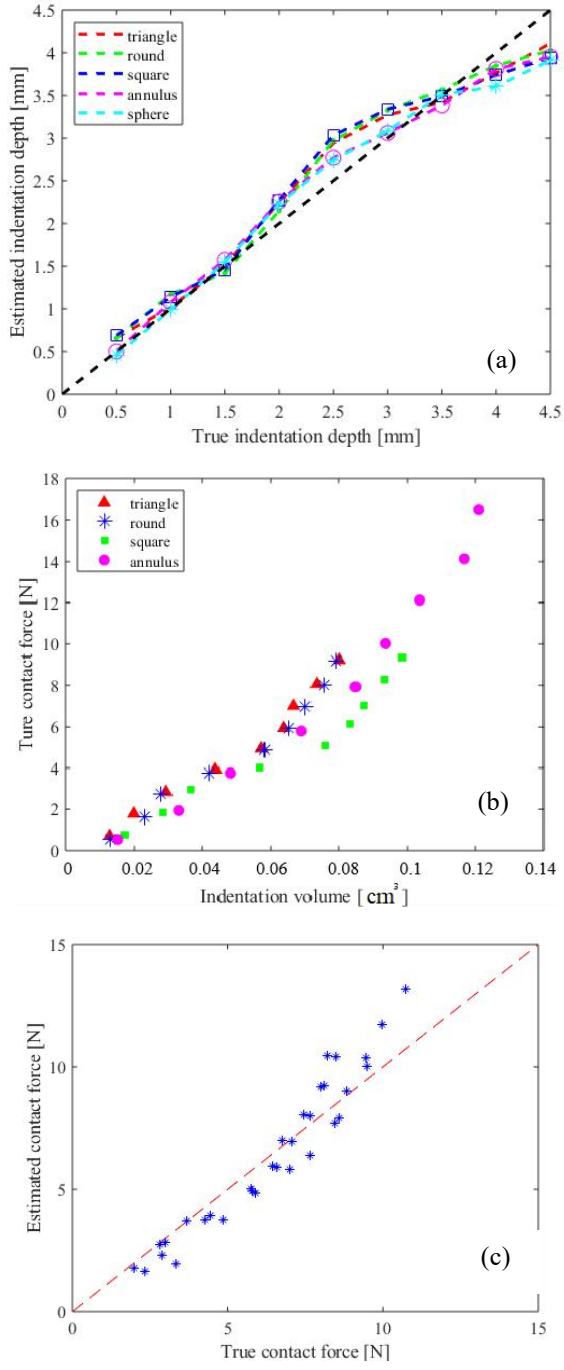

Fig. 5 (a) Indentation estimation with different shapes and depths. (b) True force value of different indentation volume. (c) Comparisons between true and estimated contact force.

For 3D reconstruction experiments, the true force values have been collected from the 6-axis force/torque sensor (ATI mini40), as shown in Fig. 3. The corresponding estimated indentation volumes have been calculated from 3D reconstruction. Then the contact force can be estimated by the corresponding indentation volume as described in Eq (6).

Fig. 5(c), the indentation volume with corresponding contact force is shown in the same graph. The data indicate a linear relationship between the two variables. Therefore, by linear fitting different data points, the estimated linear relationship can be derived, where coefficient (k) equals to 82.3 (N/cm^3). The result of the linear fitting between the indentation volume and estimated contact force shows that its SSE (sum of squared errors) is 46.52 among 40 different data samples and the MAE (mean absolute error) is 0.7072N. Subsequently, the estimated contact force for each experiment is acquired based on Eq (6).

Fig. 5(c) illustrates the relationship between indentation volume and the contact force from experiments with all the indenters. The figures indicate that the force correlates linearly with the volume change. Because the elastomer has equation (6), the area resolution and the displacement resolution. The current sensor grating design and algorithm has indentation resolution (I_s) of 0.5mm and contact area resolution (C_s) of 1mm. The theoretical force resolution $F_s = kC_sI_s \sim 0.002N$. based on the contact area of the indenters used the volume resolution is ~ $0.009cm^3$, the force sensing resolution is ~ 0.7N in this study. Based on the current sensor design, the force sensing range is from 0N to 16N and the force sensing resolution is about 4.6% of the sensing range.

C. *Temperature sensing*

To calibrate the temperature sensitivity, the sensor is put into an oven and heated from 25° C to 31° C, while a reference thermometer (Carel NTC Temperature indenter) is placed inside the oven to verify the true temperature value. For each experiment, the colour variation of the TLC layer is recorded by the camera. Two experiments were conducted. Average hue values of the pixels from the image with respect to the temperature values are analyzed to identify the mathematical relationship between hue value and temperature. At last, an annulus-shaped indenter is heated in the oven and contacted to the sensor to test the distributed temperature estimation ability of the sensing principle.

To investigate the temperature estimation ability of the sensor, the experiment setup has been placed in an oven and heated from 25℃ to 31℃. Images of the colour variation during the heating procedure as well as the corresponding real-time temperature data have been recorded. According to the principle of TLC ink, the spacing of crystal increases with the increase of temperature, which makes the wavelength reflected light decrease within visible spectrum. As shown in Fig. 6 (a), the TLC ink appear different colours under different temperatures. When the temperature increases, the colour of reflected light varies from red to purple. To avoid lighting interference when measuring the TLC colour, the images have been transferred from RGB to HSV colour space, in which the H stands for hue value of the pixels. When the lighting environment has been settled, the saturation and value of the images captured is determined. The hue value of

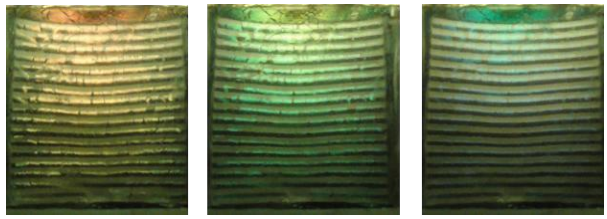

(a)

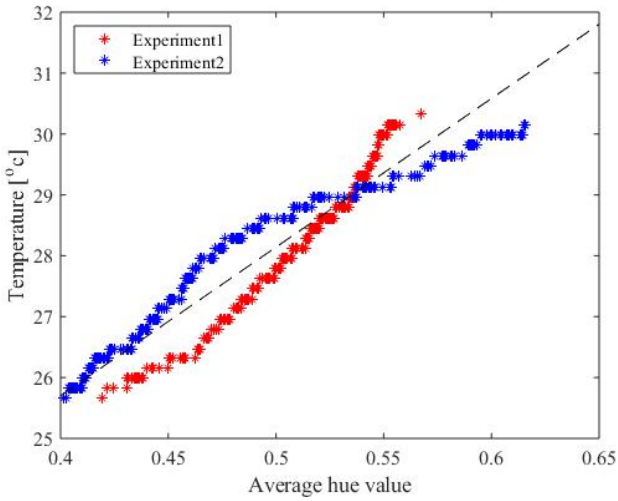

(b)

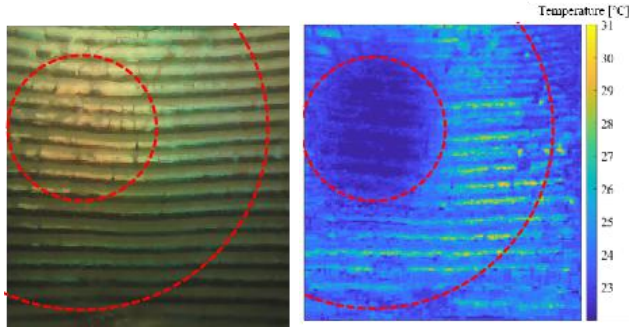

(c)

Fig. 6 (a) From left to right: images of Sensing layer in 25℃, 27℃ and 30℃. (b) Linear fitting of average hue value and temperature from experiments. (c) Local temperature estimation of the heated annulus indenter.

the reflected light increases while its wavelength decreases. Therefore, the mathematical relationship between hue value of the pixels and estimated temperature value can be established. By averaging the hue value of each frame and comparing the hue value with the true temperature value, a linear relationship can be derived.

In Fig. 6 (b), one dot represents the average hue value of pixels on one image, at a certain temperature level. The red dots and blue dots represent the results from two repeated experiments and the data from two experiments are combined to derive the temperature-hue relationship. The results from two experiments are fitted to one linear equation.Upon linearizing the temperature-hue relationship, it can be described as:

$$T = 24.19 \cdot H + 19.08 \quad (7)$$

Where T is the estimated temperature and H is hue value of pixel. In this linear fitting result, the SSE is 115 and the MAE (mean absolute error) is 0.4217℃. According to the data, the minimal hue value variation that can be recognized by the sensor is about 0.02. Therefore, it can be concluded that the temperature sensing range of this sensor is from 25℃ to 31℃ and the temperature estimation resolution of it is about 0.4℃, which is about 6.7% of the sensing range.

The outcome of the distributed temperature sensing experiment is shown in Fig. 6 (c). The dotted red circles indicate the boundary of different temperature area, which is caused by the contact of heated annulus indenter. Moreover, the geometrical shapes of the indenters can be easily indicated. Therefore, the distributed temperature sensing ability of this sensing principle can be proved.

IV. Conclusion and Discussion

The experimental results presented in this work indicate that the proposed sensing principle has the capability of determining contact shapes. From the contact force estimation experiment, the mathematical relationship between estimated indentation volume and estimated force is derived. The experimental results between estimated and true force indicate good accuracy of the equations and reliability of the image-based force estimation principle. In the temperature estimation experiment, the mathematical relationship between hue value and local temperature is described. These experiments designed for the multifunctional sensor indicate the feasibility of achieving artificial somatosensory system in a vast number of various aspects by using this sensing principle. Overall, the objectives of this sensing principle, including distributed pressure sensing and temperature sensing while maintaining a flexible sensing structure are achieved.

Compared with the existing soft tactile sensing principles based on electric components [1][5], magnetic components [9][11] and vision [13-17], the principle presented in this paper provide the extra dimension of distributed temperature sensing in addition to the tactile sensing capability offered by existing methods. The temperature sensing range and resolution can be customized by using different TLC ink. Furthermore, compared to electrical-based (resistive, capacitive sensing) and magnetic field-based sensing tactile sensing technologies [23, 24], the proposed method offers advantage of higher spatial resolutions and is resilient to electromagnetic field disturbance. Besides the temperature sensing ability, our design simplifies the lighting condition for deformation 3D reconstruction compared to Gelsight [14], and does not requires the micro pins on the underside of soft membrane as used in the Tactip sensor family [15], facilitating the fabrications and miniaturization. The sensing principle can be used in medical instruments such as surgical grippers and endoscopes. Moreover, the sensing principle presented in this paper provides the feasibility of achieving human-skin like tactile sensing in robotic hands.

However, there are a number of technical hurdles need to be addressed in the future. Similar to the other vision-based tactile sensing principles, the sampling frequencies and resolutions of sensors are limited by the quality of cameras. Higher frame rate and high image resolution increases the cost and the size of camera. Thus, how to achieve sensor miniaturization while keep high performance and low cost is still an open question. In addition, the TLC layer used in the sensor is fragile when undertaking high frequency compression force. To improve the robustness of temperature sensing principle, new TLC material with higher elasticity need to be explored. Moreover, to thoroughly eliminate the interference between temperature and pressure sensing, one possible solution is converting original image into binary image. Therefore, a suitable threshold that used to convert the grayscale image to binary image will be selected in the future. More experiments will be implemented to ensure that the threshold will not influence the contact force resolution.

References

[1] Lee, H., Park, K., Kim, Y., & Kim, J. (2017, March). Durable and repairable soft tactile skin for physical human robot interaction. In Proceedings of the Companion of the 2017 ACM/IEEE International Conference on Human-Robot Interaction (pp. 183-184). ACM.

[2] Dahiya, R. S., Metta, G., Valle, M., & Sandini, G. (2009). Tactile sensing—from humans to humanoids. IEEE transactions on robotics, 26(1), 1-20.

[3] Hirai, Y., Suzuki, Y., Tsuji, T., & Watanabe, T. (2018, April). Tough, bendable and stretchable tactile sensors array for covering robot surfaces. In 2018 IEEE International Conference on Soft Robotics (RoboSoft) (pp. 276-281). IEEE.

[4] Büscher, G. H., Kõiva, R., Schürmann, C., Haschke, R., & Ritter, H. J. (2015). Flexible and stretchable fabric-based tactile sensor. Robotics and Autonomous Systems, 63, 244-252.

[5] Rana, A., Roberge, J. P., & Duchaine, V. (2016). An improved soft dielectric for a highly sensitive capacitive tactile sensor. Ieee sensors journal, 16(22), 7853-7863.

[6] Zhang, H., Wang, M. Y., Li, J., & Zhu, J. (2016). A soft compressive sensor using dielectric elastomers. Smart Materials and Structures, 25(3), 035045.

[7] Weerasinghe, L., & Chathuranga, D. S. (2018, May). Development and Characterization of a Soft Tactile Sensor Array Used for Parallel Grippers. In 2018 Moratuwa Engineering Research Conference (MERCon) (pp. 102-107). IEEE.

[8] Boer, G. D., Raske, N., Wang, H., Kow, J., Alazmani, A., Ghajari, M., ... & Hewson, R. (2017). Design optimisation of a magnetic field based soft tactile sensor. Sensors, 17(11), 2539.

[9] Paulino, T., Ribeiro, P., Neto, M., Cardoso, S., Schmitz, A., Santos-Victor, J., ... & Jamone, L. (2017, May). Low-cost 3-axis soft tactile sensors for the human-friendly robot Vizzy. In 2017 IEEE International Conference on Robotics and Automation (ICRA) (pp. 966-971). IEEE.

[10] Jamone, L., Natale, L., Metta, G., & Sandini, G. (2015). Highly sensitive soft tactile sensors for an anthropomorphic robotic hand. IEEE sensors Journal, 15(8), 4226-4233.

[11] Nagahama, S., Migita, K., & Sugano, S. (2019). Soft Magnetic Powdery Sensor for Tactile Sensing. Sensors, 19(12), 2677.

[12] Sferrazza, C., & D'Andrea, R. (2019). Design, Motivation and Evaluation of a Full-Resolution Optical Tactile Sensor. Sensors, 19(4), 928.

[13] Donlon, E., Dong, S., Liu, M., Li, J., Adelson, E., & Rodriguez, A. (2018, October). GelSlim: A High-Resolution, Compact, Robust, and Calibrated Tactile-sensing Finger. In 2018 IEEE/RSJ International Conference on Intelligent Robots and Systems (IROS) (pp. 1927-1934). IEEE.

[14] Johnson, M., Cole, F., Raj, A., & Adelson, E. (2011). Microgeometry capture using an elastomeric sensor. ACM Transactions On Graphics, 30(4), 1.

[15] Ward-Cherrier, B., Pestell, N., Cramphorn, L., Winstone, B., Giannaccini, M. E., Rossiter, J., & Lepora, N. F. (2018). The tactip family: Soft optical tactile sensors with 3d-printed biomimetic morphologies. Soft robotics, 5(2), 216-227.

[16] Van Duong, L., Asahina, R., & Wang, J. (2019, April). Development of a Vision-Based Soft Tactile Muscularis. In 2019 2nd IEEE International Conference on Soft Robotics (RoboSoft) (pp. 343-348). IEEE.

[17] Zhang, T., Cong, Y., Li, X., & Peng, Y. (2018, July). Robot Tactile Sensing: Vision Based Tactile Sensor for Force Perception. In 2018 IEEE 8th Annual International Conference on CYBER Technology in Automation, Control, and Intelligent Systems (CYBER) (pp. 1360-1365). IEEE.

[18] Takeda, M., & Mutoh, K. (1983). Fourier transform profilometry for the automatic measurement of 3-D object shapes. Applied optics, 22(24), 3977-3982.

[19] Su, X., & Chen, W. (2000, October). Fourier transform profilometry for dynamic 3D shape. In Process Control and Inspection for Industry (Vol. 4222, pp. 245-248). International Society for Optics and Photonics.

[20] Dong, H. (2013). The measurement of 3D object shape based on Fourier Transform Profilometry. In Advanced Materials Research (Vol. 756, pp. 678-681). Trans Tech Publications.

[21] Collings, P. J., & Hird, M. (2017). Introduction to liquid crystals: chemistry and physics. CRC Press.

[22] Sage, I. (2011). Thermochromic liquid crystals. Liquid crystals, 38(11-12), 1551-1561.

[23] Acer, M., Yıldız, A. F., & Bazzaz, F. H. (2017, October). Development of a soft PZT based tactile sensor array for force localization. In 2017 XXVI International Conference on Information, Communication and Automation Technologies (ICAT) (pp. 1-6). IEEE.

[24] Wang, H., de Boer, G., Kow, J., Ghajari, M., Alazmani, A., Hewson, R., & Culmer, P. (2016). A low-cost soft tactile sensing array using 3D Hall sensors. Procedia Engineering, 168, 650-653.

[25] Winstone, B., Griffiths, G., Pipe, T., Melhuish, C., & Rossiter, J. (2013, July). TACTIP-tactile fingertip device, texture analysis through optical tracking of skin features. In Conference on Biomimetic and Biohybrid Systems (pp. 323-334). Springer, Berlin, Heidelberg.

[26] Yuan, W., Li, R., Srinivasan, M. A., & Adelson, E. H. (2015, May). Measurement of shear and slip with a GelSight tactile sensor. In 2015 IEEE International Conference on Robotics and Automation (ICRA) (pp. 304-311). IEEE.